HHS Public Access

Author manuscript

ACS Appl Mater Interfaces. Author manuscript; available in PMC 2018 November 08.

Published in final edited form as:

ACS Appl Mater Interfaces. 2017 November 08; 9(44): 38304–38312. doi:10.1021/acsami.7b12216.

Radiolabeled, antibody-conjugated manganese oxide nanoparticles for tumor vasculature targeted positron emission tomography and magnetic resonance imaging

Yonghua Zhan[†,#], **Sixiang Shi**[‡,#], **Emily B. Ehlerding**[§], **Stephen A. Graves**[§], **Shreya Goel**[‡], **Jonathan W. Engle**[§], **Jimin Liang**[§,†], **Jie Tian**[‖,*], and **Weibo Cai**[*,‡,⊥]

[†]Engineering Research Center of Molecular and Neuro Imaging of the Ministry of Education, School of Life Science and Technology, Xidian University, Xi'an, Shaanxi, 710071, China

[‡]Department of Radiology, University of Wisconsin–Madison, WI, 53705,USA

[§]Department of Medical Physics, University of Wisconsin-Madison, WI, 53705,USA

[‖]Institute of Automation, Chinese Academy of Sciences, Beijing, 100190, China

[⊥]University of Wisconsin Carbone Cancer Center, Madison, WI, 53705, USA

Abstract

Manganese oxide nanoparticles (Mn_3O_4 NPs) have attracted a great deal of attention in the field of biomedical imaging because of their ability to create an enhanced imaging signal in MRI as novel potent T_1 contrast agents. In this study, we present tumor vasculature-targeted imaging in mice using Mn_3O_4 NPs through conjugation to the anti-CD105 antibody TRC105 and radionuclide copper-64 (^{64}Cu, $t_{1/2}$: 12.7 h). The Mn_3O_4 conjugated NPs, ^{64}Cu-NOTA-Mn_3O_4@PEG-TRC105, exhibited sufficient stability *in vitro* and *in vivo*. Serial positron emission tomography (PET) and magnetic resonance imaging (MRI) studies evaluated the pharmacokinetics and demonstrated targeting of ^{64}Cu-NOTA-Mn_3O_4@PEG-TRC105 to 4T1 murine breast tumors *in vivo*, compared to ^{64}Cu-NOTA-Mn_3O_4@PEG. The specificity of ^{64}Cu-NOTA-Mn_3O_4@PEG-TRC105 for the vascular marker CD105 was confirmed through *in vivo*, *in vitro*, and *ex vivo* experiments. Since Mn_3O_4 conjugated NPs exhibited desirable properties for T_1 enhanced imaging and low toxicity, the tumor-specific Mn_3O_4 conjugated NPs reported in this study may serve as promising multifunctional nanoplatforms for precise cancer imaging and diagnosis.

Graphical abstract

[*]Corresponding Authors: wcai@uwhealth.org (W. Cai); tian@ieee.org (J. Tian).
[#]These authors contributed equally.

Supporting Information

The Supporting Information is available free of charge on the ACS Publications website, which contains UV-Vis absorbance spectra, DLS measurements, cell viability assays, and ICP-AES analysis of tissue biodistribution.

Author Contributions

The manuscript was written with contributions from all authors. All authors have given approval of the final version of the manuscript.

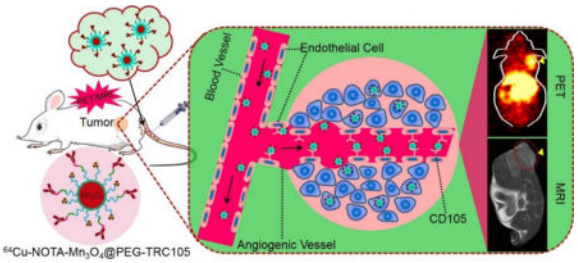

Keywords

Manganese oxide nanoparticles; Cancer; Positron emission tomography (PET); Magnetic resonance imaging (MRI); CD105 (endoglin)

INTRODUCTION

Medical imaging techniques have come to play an important role in the early detection and diagnosis of disease due to their precise diagnostic abilities at the whole-body, molecular, and cellular levels.[1,2] Various imaging technologies in widespread use today include computed tomography (CT), positron emission tomography (PET), magnetic resonance imaging (MRI), ultrasound (US), single-photon emission computed tomography (SPECT) and photoacoustic imaging (PA).[3] Because each of these modalities has its own unique strengths and limitations regarding spatial and temporal resolution, tissue penetration depth, detection sensitivity, and cost, combinations of different imaging modalities are being developed and have shown promise to overcome clinical diagnostic challenges. Among these combinations, the use of PET and MRI together has been under vigorous development and is currently in clinical trials for applications in cancer detection thanks to the high sensitivity of PET and ultra-high spatial resolution of MRI.[4, 5]

To further make full use of PET/MR imaging, creation of dual-modal PET/MR imaging probes has been actively pursued since their emergence in the last decade.[6–8] T_1-positive paramagnetic and T_2-negative super paramagnetic nanoparticles are among commonly-used MRI contrast components. In particular, T_2 contrast agents based on iron oxide have been widely used as the MRI contrast moeity in PET/MRI probes over the last two decades and a few have advanced into clinical trials or received the approval of the United States' Food and Drug Administration.[9–12] However, these nanoparticles have been somewhat limited in clinical applications due to their drawbacks of negative contrast and high susceptibility; therefore, it is desirable to develop new PET/MRI probes with higher T_1 or T_2 relaxivity components.

T_1 contrast agents based on gadolinium and manganese in the form of ionic complexes or colloidal nanoparticles have gained increased interest because of their signal-enhancing positive contrast characteristics.[2, 13] However, the complex-based agents demonstrate downfalls such a relatively short vascular residence time and notable toxicity *in vivo*, which limit their extensive clinical application in disease diagnosis.[13] In view of this, recent manganese (II)-based nanoparticles have been considered promising T_1-weighted contrast

agents, attributed to their relatively high magnetization spins and fast water proton exchange rates.[14] Meanwhile, the manganese (II)-based agents also exhibit low side effects and good biocompatibility as manganese itself is an essential component of cells and a cofactor for many enzymes.[15] Most importantly, monodisperse manganese-based nanoparticles of good crystallinity and uniformity have been demonstrated to be easily synthesized on a large scale under mild and ambient reaction conditions.[16] This class of MRI contrast agents, particularly manganese oxides, indicates a promising new direction in biomedical imaging and tumor-targeted diagnosis.[17,18] Multimodality imaging probes and their application in biomedical imaging have been reported in recent years. For instance, solid and hollow MnO nanoparticle-based T_1 contrast agents have been reported for selectively imaging breast cancer cells and for drug delivery by several groups.[19–24] Yang and co-workers further developed silica-coated Mn_3O_4 core-shell nanoparticles for tumor folate-receptor-targeted MRI and fluorescent imaging *in vitro* and tumor aptamer-receptor-targeted MRI imaging *in vivo*.[25–27] Although the reported manganese-based NPs have exhibited good imaging capabilities as contrast agents, it is still urgent to develop novel multifunctional manganese-based imaging probes for future biomedical imaging, especially PET/MRI probes. As we all know, driven by the impending clinical requirement, the perfect combination of PET and MRI has been under rapid development in clinical cancer detection and diagnosis due to the high sensitivity of PET and ultra-high spatial resolution of MRI. Inspired by this, we were encouraged to develop a new PET/MRI imaging probe with a manganese oxide-based T_1 contrast component and Cu-64 positron emission for *in vivo* tumor imaging.

Effective delivery of agents to specific sites in the body is a major barrier to tumor imaging and therapy.[28–30] Compared to tumor cell-based targeting, targeting of nanoparticles to tumor vasculature is more reasonable due to the relative ease of access for nanoparticles to vasculature after intravenous injection. Additionally, extravasation is not required (as this is a known issue with many nanoplatforms). Furthermore, angiogenesis, or the formation of new blood vessels, is a critical process in tumor development and progression.[31–34] CD105 (also called endoglin) is nearly exclusively expressed on proliferating endothelial cells, which are a strong marker for tumor angiogenesis.[32–34] More importantly, various studies have confirmed that, in more than ten solid tumor types, high expression of CD105 is correlated with poor patient outcomes, which makes it a widely-applicable target in cancer.[35–38] Using TRC105 (a chimeric IgG1 monoclonal antibody which binds to both human and murine CD105[39,40]) as the targeting ligand, our group has monitored CD105 expression using both antibody and nanoplatforms, demonstrating the great potential of CD105-targeted agents for future extensive applications in cancer diagnosis and therapy.[41–47] Inspired by this previous success, we set out to develop our first PET/MRI probe targeted to CD105.

In this work, we investigated *in vivo* tumor vasculature targeting with surface functionalized Mn_3O_4 nanoparticles. We utilized a mild and ambient reaction method to synthesize uniform Mn_3O_4 nanocrystals, and subsequently conjugated them with TRC105 and S-2-(4-isothiocyanatobenzyl)-1,4,7-triazacyclononane-1,4,7-triacetic acid (p-SCN-Bn-NOTA) through polyethylene glycol (PEG) linkers, for radiolabeling with ^{64}Cu (half-life: 12.7 h) to form the ^{64}Cu-NOTA-Mn_3O_4@PEG-TRC105 conjugate (Scheme 1). To demonstrate the CD105 specificity of ^{64}Cu-NOTA-Mn_3O_4@PEG-TRC105, *in vivo* PET/MRI imaging,

biodistribution, and blocking studies were carried out in 4T1 tumor-bearing mice, the results of which were further validated by additional *in vitro* and *ex vivo* experiments. Moreover, serum biochemistry assays and histological assessments were also conducted to determine the potential toxicity of these nanoparticles.

2 MATERIALS AND METHODS

2.1. Reagents

Oleylamine (approximate C18-content 80–90%), oleic acid (technical grade 90%), xylene (98%), manganese (II) acetate (98%), CCK-8 and fluorescein isothiocyanate (FITC) were obtained from Sigma-Aldrich. S-2-(4-isothiocyanatobenzyl)-1, 4, 7-triazacyclononane-1, 4, 7-triacetic acid (p-SCN-Bn-NOTA) was purchased from Macrocyclics, Inc. (Dallas, TX). TRC105 was supplied by TRACON Pharmaceuticals Inc. (San Diego, CA). DSPE-PEG_{5000}-NH_2 and SCM-PEG_{5000}-Mal were purchased from Creative PEGworks (Winston Salem, NC). AlexaFluor488- or Cy3-labeled secondary antibodies (Jackson Immunoresearch Laboratories, Inc., West Grove, CA), rat anti-mouse CD31 primary antibody (BD Biosciences, San Diego, CA), and PD-10 desalting columns (GE Healthcare, Piscataway, NJ) were all acquired from commercial sources. All buffers and water were of Millipore grade. All other reaction buffers and chemicals were obtained from Thermo Fisher Scientific (Fair Lawn, NJ).

2.2. Synthesis of the Mn_3O_4 NPs

Mn_3O_4 NPs were prepared according to a previously reported method with slight modifications.[16] The nanoparticles were modified with DSPE-PEG_{5000}-NH_2 to obtain Mn_3O_4@PEG-NH_2 NPs. Mn_3O_4@PEG-NH_2 was then reacted with p-SCN-Bn-NOTA or FITC as described previously,[45] at a molar ratio of 1:10 at pH 8.5 for 3 h. The nanoparticles were then further modified through the addition of SCM-PEG-Mal using similar procedures. In preparation for further reactions, TRC105 was incubated with Traut's reagent at a molar ratio of 1:25 at pH 8.0 for 2 h. The final products (NOTA-Mn_3O_4@PEG-TRC105 or FITC-Mn_3O_4@PEG-TRC105) were generated as described previously.[48] Final purification to remove excess TRC105 was achieved by passing the solution through a PD-10 size-exclusion column.

2.3. Characterization

The size and morphology of Mn_3O_4 NPs were determined using a JEOL JEM-2100 transmission electron microscope (TEM). X-ray diffraction (XRD) measurements were conducted on a Bruker D4 diffractometer. The surface zeta potential and hydrodynamic size were measured using a Malvern Zetasizer Nano ZS. The T_1-relaxivities and T_1 images were obtained with a conventional spin echo acquisition (repetition time, TR, 1000 ms) with echo time, TE, of 50 ms, and a section thickness of 1 mm in a 4.7 T small animal scanner (Agilent Technologies, Santa Clara, CA). Relaxivity values of r_1 were calculated through curve fitting of $1/T_1$ (s^{-1}) *versus* the manganese concentration (mM). The concentration of Mn was determined by ICP-AES (VISTAMPXICP Varian, USA).

2.4. Radiolabeling and serum stability studies

Cu-64 was produced using a GE PETrace cyclotron. 50 μg of NOTA-Mn_3O_4@PEG-TRC105 or NOTA-Mn_3O_4@PEG was mixed with $^{64}CuCl_2$ (74 MBq), and the reaction proceeded at 37°C for 30 min, with the reaction and purification proceeding as outlined previously.[38] To ensure that ^{64}Cu-NOTA-Mn_3O_4@PEG-TRC105 and ^{64}Cu-NOTA-Mn_3O_4@PEG were stable for *in vivo* applications, serum stability studies were performed. ^{64}Cu-NOTA-Mn_3O_4@PEG-TRC105 or ^{64}Cu-NOTA-Mn_3O_4@PEG were incubated in complete mouse serum at 37 °C for 48 h, and analysis was performed as previously described.[46]

2.5. Cell lines and animal model

4T1 murine breast cancer, human embryonic kidney 293 cells (HEK-293), human hepatoma cells (HUH-7), MCF-7 human breast cancer cells, and human umbilical vein endothelial cells (HUVECs) were obtained from the American Type Culture Collection (ATCC, Manassas, VA). Cells were cultured and 4T1 animal models were developed as previously described.[46]

2.6. In vitro cytotoxicity assay

The cytotoxicity of Mn_3O_4 conjugated NPs was assessed with a CCK-8 assay using HUH-7 cells and HEK-293 cells.[47] Briefly, cells were seeded in 96-well plates at 20,000 cells per well in 200 μL culture medium. The cells were maintained in RPMI-1640 containing 10% fetal bovine serum (FBS) and incubated at 37 °C in a humidified cell culture incubator with 5% CO_2 atmosphere for 24 h. Mn_3O_4 conjugated NPs solutions with different concentrations from 200 to 1000 μg/mL were added to each well, and the cells were subjected to a CCK-8 assay after being incubated for another 24 h. The cell viability was determined through measuring the absorption at 450 nm using a microplate reader. Cell viability was calculated using: cell viability (%) = (mean absorption value of treatment group/mean absorption value of control) ×100.

2.7. Flow cytometry

HUVECs (CD105 positive) and MCF-7 cells (CD105 negative) were harvested and incubated with FITC-Mn_3O_4@PEG-TRC105 or FITC-Mn_3O_4@PEG for flow cytometry analysis as described elsewhere.[41,46] A blocking study was also performed in which cells were pre-incubated with 500 μg/mL of TRC105 prior to incubation with the nanoparticles. All cells were then analyzed using a BD FACSCalibur cytometer (Bectone-Dickinson, San Jose, CA) and FlowJo analysis software (Tree Star, Inc., Ashland, OR).

2.8. PET imaging and ex vivo biodistribution studies

PET scans of 4T1 tumor-bearing mice (n = 3 per group) at 0.5, 3, 6, and 24 h post-injection (p.i.) of ^{64}Cu-NOTA-Mn_3O_4@PEG-TRC105 or ^{64}Cu-NOTA-Mn_3O_4@PEG (5–10 MBq) were performed using an Inveon rodent model microPET/microCT scanner (Siemens Medical Solutions USA, Inc.) following tail vein injection. Detailed procedures for data acquisition and analysis have been reported previously.[46] Blocking studies, in which 4T1-bearing mice were injected with 1 mg of TRC105 2 h before the injection of ^{64}Cu-NOTA-Mn_3O_4@PEG-TRC105, were also carried out to confirm the *in vivo* specificity of the

nanoparticles. Quantitative data from imaging and biodistribution studies are presented as percent of the injected dose per gram of tissue (%ID/g). To further validate the PET uptake values, *ex vivo* biodistribution studies were performed both at 6 and 24 h, at the time of peak tumor uptake and the terminal imaging timepoint, respectively, as previously reported.[47]

2.9. In vivo T_1 MRI imaging

To detect Mn_3O_4 accumulation in tumors, *in vivo* T_1-weighted MR imaging was performed at 6 h post-injection after intravenous injection of 400 μL NOTA-Mn_3O_4@PEG-TRC105 with a Mn concentration of 1.04 mM. Meanwhile, a blocking study was also conducted through injection of 1 mg of TRC105 before NOTA-Mn_3O_4@PEG-TRC105 administration and subsequent MRI imaging at 6 h p.i. using a 4.7 T small animal scanner (Agilent Technologies, Santa Clara, CA) with the following parameters: TR = 500 ms; TE = 12 ms; flip angle = 120°; FOV = 40 mm × 40 mm; matrix = 256 × 256; NEX = 8; slice thickness = 1 mm for axial images.

2.10. Histology

Three 4T1-bearing mice were each injected with NOTA-Mn_3O_4@PEG-TRC105 (5 mg/kg dose) and euthanized 6 h p.i. of the nanoparticles. The tumor, spleen, liver, and muscle were harvested, frozen, and sectioned for histological analysis as previously described.[41, 45] Rat anti-mouse CD31 and Cy3-labeled donkey anti-rat antibodies served to visualize vasculature, while an AlexaFluor488-labeled goat anti-human antibody allowed staining of TRC105 in the nanoparticles. All images were acquired using a Nikon Eclipse Ti microscope.

2.11. In Vivo Biocompatibility Studies of Mn_3O_4 NPs

The toxicity of Mn_3O_4@PEG NPs to healthy male BALB/c mice was evaluated through injection of Mn_3O_4@PEG NPs (dose: 20 mg/kg) *via* the tail vein. Mice injected with PBS alone served as a control group (n = 3). Mice were sacrificed on Day 7 and Day 14 for blood serum biochemistry assays. At the same time, major organs from each mouse (heart, liver, spleen, lung, and kidney) were harvested and fixed in 4% paraformaldehyde solution for 1 day. These tissues were then embedded in paraffin, sliced, and stained with hematoxylin and eosin (H&E) and examined using a digital microscope (Leica DM5000). The serum chemistry data, including hepatic and kidney functions, was measured by the University of Wisconsin-Madison Veterinary Hospital.

3. RESULTS AND DISCUSSION

3.1. Synthesis and characterization of Mn_3O_4 conjugated NPs

As shown in Scheme 1, Mn_3O_4 conjugated NPs (^{64}Cu-NOTA-Mn_3O_4@PEG-TRC105) were prepared according to our previous report.[16,42,47] When it comes to the preparation of monodispersed Mn_3O_4 NPs, various methods have been reported such as solvothermal,[48] oxidation-precipitation,[49] thermal decomposition,[27] surfactant-assisted synthesis,[50] microwave irradiation[51] and vapor phase growth.[52] However, it is still difficult to synthesize uniform Mn_3O_4 NPs to meet the desired biomedical requirements. Fortunately, Hyeon and co-workers developed a new simple method to prepare Mn_3O_4 NPs with various shapes at

low temperature in air atmosphere.[16] Thus, in this present work, an improved method was used to prepare Mn_3O_4 NPs according to the method by Hyeon. Based on TEM measurements, Mn_3O_4 NPs were monodispersed in nonpolar organic solvent and had a small spherical shape of approximately 7 nm (Figure 1a), which was consistent with the previous reports.[16,26,27] Furthermore, the hydrophobic Mn_3O_4 NPs were successfully transferred to the aqueous phase by coating with amine-functionalized PEG lipids (DSPE-PEG_{5000}-NH_2) and showed good stability in aqueous solution (Figure 1b). In addition, DLS measurements showed that Mn_3O_4@PEG-NH_2 has a hydrodynamic diameter of 11 ± 3.5 nm, whereas the diameter of Mn_3O_4 NPs is 8 ± 4.6 nm (Figure 1d), which was similar to the observation from TEM. The zeta-potential value of Mn_3O_4@PEG-NH_2 was −21.7 ± 2.3 mV. The crystallography of the Mn_3O_4 NPs was further verified by powder XRD (Figure 1c), which showed that all the diffraction peaks of the Mn_3O_4 NPs can be indexed as a tetragonal Mn_3O_4 phase (Joint Committee for Powder Diffraction Standards (JCPDS) card no: 24-0734).

After further conjugation as previously reported,[46] the zeta-potential values changed significantly to −14.8 ± 3.7 mV (NOTA-Mn_3O_4@PEG) and −3.2 ± 4.8 mV (NOTA-Mn_3O_4@PEG-TRC105), suggesting successful conjugation of NOTA and TRC105 to the surface of Mn_3O_4@PEG-NH_2. Moreover, in order to further confirm the conjugation, the absorption spectra of the TRC105, Mn_3O_4@PEG and NOTA-Mn_3O_4@PEG-TRC105 were measured by UV spectrophotometer. It can be seen that the TRC105 and NOTA-Mn_3O_4@PEG-TRC105 NPs have obvious absorption peaks at 280 nm (Figure S1), which were ascribed to the protein itself. Furthermore, the size of NOTA-Mn_3O_4@PEG was also increased from 11 ± 3.5 nm to 32.6 ± 4.5 nm, which was attributed to the diameter of TRC105 itself (Figure S2). An estimated average of 1.67 TRC105 antibodies were conjugated to each nanoparticle.

To examine the MRI contrast capabilities of the Mn_3O_4 conjugated NPs, the relaxation properties of Mn_3O_4@PEG-NH_2 and NOTA-Mn_3O_4@PEG-TRC105 in aqueous solution were measured by a 4.7 T MRI scanner. It was clear that both NOTA-Mn_3O_4@PEG-TRC105 and Mn_3O_4@PEG displayed signal enhancement in T_1-weighted MR images with increasing manganese concentration (Figure 2a). The r_1 values of the NOTA-Mn_3O_4@PEG-TRC105 and Mn_3O_4@PEG-NH_2 were calculated as 0.54 $mM^{-1}s^{-1}$ and 0.57 $mM^{-1}s^{-1}$ respectively, from linear fitting of $1/T_1$ versus Mn^{2+} concentration (Figure 2b). These values are also similar to those of previously-reported Mn_3O_4 NPs, verifying their potential use as positive MRI contrast agents.[22, 25–27] Other T_1 contrast agents (such as those based on gadolinium) certainly possess higher r_1 values; however, the promise of Mn-based agents lies in their relatively lower toxicity concerns. This study demonstrates that Mn-based nanoparticles do indeed provide MRI contrast; however, there certainly is room for improvement in their r_1 values.

3.2. Flow cytometry and serum stability studies

HUVECs (CD105 positive) and MCF-7 cells (CD105 negative) were incubated in PBS containing NOTA-Mn_3O_4@PEG-TRC105 NPs at different concentrations and analyzed using flow cytometry. As shown in Figure 3a, the fluorescence signal of CD105 positive

HUVECs was approximately 18 fold higher than that of the untreated cells upon incubation with FITC-Mn_3O_4@PEG-TRC105, whereas no fluorescence signal enhancement was observed in the blocking and FITC-Mn_3O_4@PEG treatment groups. In addition, MCF-7 cells, which are CD105 negative, demonstrated minimal fluorescence across all groups. Taken together, the results of flow cytometry indicate high CD105 specificity and minimal non-specific binding of TRC105-conjugated Mn_3O_4 NPs.

The stability of ^{64}Cu labeling was evaluated through a serum stability study of ^{64}Cu-NOTA-Mn_3O_4@PEG-TRC105. As shown in Figure 3b, after incubation in complete mouse serum at 37 °C for 24 h, nearly 80% of ^{64}Cu remained on the Mn_3O_4 conjugated NPs, suggesting good stability of the radiolabel on the Mn_3O_4 conjugated NPs. Good radio-stability in serum indicated that ^{64}Cu-NOTA-Mn_3O_4@PEG-TRC105 would have desirable properties *in vivo*.

3.3. Cytotoxicity assay

The cytotoxicity of Mn_3O_4 conjugated NPs was evaluated by CCK-8 assay with normal cells (HEK-293) and tumor cells (HUH-7). No obvious cytotoxicity of Mn_3O_4 conjugated NPs to HEK-293 and HUH-7 cells was observed at any studied concentration (from 200 to 1000 μg mL^{-1}, Figure S3) or any timepoint (24 or 48 h). Even at the concentration of 1000 μg mL^{-1}, the viability for both HEK-293 and HUH-7 cells remained above 80%, indicating that the Mn_3O_4 conjugated NPs should have little cytotoxicity at the given concentration range.

3.4. PET imaging and biodistribution studies

Since many nanomaterials extravasate poorly, targeting to the tumor vasculature is a promising strategy for tumor targeting. CD105 is an ideal marker primarily expressed on tumor neovasculature, and thus can serve as an attractive and universal vascular target for multiple solid tumor types.[37, 38] Additionally, the 4T1 model is a fast-growing tumor that exhibits very high levels of angiogenesis, making targeting to CD105 quite simple. In view of this, the specific targeting capability of ^{64}Cu-NOTA-Mn_3O_4@PEG-TRC105 was evaluated through PET imaging. As Cu-64 has a 12.7 h half-life, serial PET scans were performed at time points of 0.5, 3, 6 and 24 h p.i., as seen in Figure 4. The quantitative data obtained from the PET scans are shown in Figure 5a, b and c. Since the hydrodynamic diameter of the Mn_3O_4 conjugated NPs is above the cutoff for renal filtration,[53] these nanoparticles were mainly cleared through the hepatobiliary pathway. The liver uptake of ^{64}Cu-NOTA-Mn_3O_4@PEG-TRC105 was 25.3 ± 2.5, 24.1 ± 1.3, 23.2 ± 0.5 and 21.6 ± 0.7 %ID/g at 0.5, 3, 6, and 24 h p.i. respectively, while the blood pool radioactivity was 4.8 ± 0.8, 3.5 ± 0.7, 3.7 ± 0.6, and 3.2 ± 0.4 %ID/g at the same timepoints (n = 3; Figure 5a), suggesting a short circulation half-life (< 30 min). More importantly, the 4T1 tumor was clearly visible after ^{64}Cu-NOTA-Mn_3O_4@PEG-TRC105 injection at 0.5 h p.i. (Figure 5a) and remained visible over time (5.8 ± 0.6, 7.8 ± 0.4, and 6.1 ± 0.2 %ID/g at 3, 6 and 24 h p.i. respectively; n = 3; Figure 5a). Pre-injection of a blocking dose of TRC105 was found to significantly reduce the tumor uptake of ^{64}Cu-NOTA-Mn_3O_4@PEG-TRC105 to 1.5 ± 0.3, 2.1 ± 0.7, 2.8 ± 0.5, and 2.0 ± 0.8 %ID/g at 0.5, 3, 6, and 24 h p.i. respectively (n = 3; Figure 5c and 5d; $p < 0.05$ at all time points), which demonstrated *in vivo* specificity of ^{64}Cu-NOTA-Mn_3O_4@PEG-TRC105 for CD105 on tumor vasculature.

Uptake of the radiolabeled nanoparticle in the liver of the blocking group was similar to mice injected with ^{64}Cu-NOTA-Mn_3O_4@PEG-TRC105 alone, at 23.9 ± 1.2, 22.3 ± 1.3, 21.2 ± 1.3 and 20.9 ± 0.3 %ID/g at 0.5, 3, 6, and 24 h p.i. (n = 3; Figure 5c). Blood pool activity (3.3 ± 0.3, 3.1 ± 0.6, 2.8 ± 0.3 and 2.3 ± 0.2 %ID/g at 0.5, 3, 6, and 24 h p.i. respectively; n = 3; Figure 5c), was slightly impacted by the excess TRC105. The 4T1 tumor uptake of ^{64}Cu-NOTA-Mn_3O_4@PEG (2.3 ± 0.3, 3.5± 0.2, 4.5 ± 0.4, and 3.1 ± 0.3 %ID/g at 0.5, 3, 6, and 24 h p.i. respectively; n = 3; Figure 5b, d) was ~ 1.5 fold lower than that of the targeted tracer, suggesting that the conjugation of TRC105 to Mn_3O_4 NPs clearly enhanced tumor uptake through binding to CD105. In addition, liver uptake (25.2 ± 1.9, 24.7 ± 1.3, 23.7 ± 1.2 and 21.3 ± 0.5 %ID/g at 0.5, 3, 6, and 24 h p.i. respectively; n = 3; Figure 5b) and radioactivity in the blood (4.4 ± 0.4, 3.6 ± 0.6, 3.8± 0.3, and 3.5 ± 0.3 %ID/g at 0.5, 3, 6, and 24 h p.i. respectively; n = 3; Figure 5b) for the nonspecific tracer were similar to those of mice injected with ^{64}Cu-NOTA-Mn_3O_4@PEG-TRC105.

Biodistribution studies of ^{64}Cu-NOTA-Mn_3O_4@PEG-TRC105 were carried out at 24 h p.i. (Figure 5e). The analysis based on both PET data and biodistribution studies were in agreement, confirming that *in vivo* serial PET imaging reflected the distribution of ^{64}Cu-NOTA-Mn_3O_4@PEG-TRC105 and ^{64}Cu-NOTA-Mn_3O_4@PEG in tumor-bearing mice. As these intravenously-injected nanomaterials are cleared through the hepatobiliary pathway, substantial radioactive content was commonly detected in the liver, intestine and spleen. To determine the fate of the nanoparticles themselves (rather than the radiolabel) in mice, quantitative biodistribution of NOTA-Mn_3O_4@PEG-TRC105 was investigated through the detection of manganese by ICP-AES at 24 h (Figure S4). After collection of the tumor, heart, liver, spleen, lung, kidney, blood, feces and urine and ICP-AES analysis, the reasonably efficient active targeting property of NOTA-Mn_3O_4@PEG-TRC105 NPs was confirmed, in accordance with the biodistribution of ^{64}Cu by gamma counter at the same time. Importantly, the tumor uptake of ^{64}Cu-NOTA-Mn_3O_4@PEG-TRC105 was significantly higher than that of ^{64}Cu-NOTA-Mn_3O_4@PEG and the blocking group, indicating that using TRC105 as a targeting ligand to vascular CD105 could effectively improve the tumor uptake.

3.5. MR imaging in vivo

While PET imaging provides high sensitivity and quantitative capabilities, essential anatomical information is also indispensable for accurate tumor imaging.[4] To further supplement the PET results, MRI was used to investigate the Mn_3O_4 conjugated NPs in 4T1 tumor-bearing mice. As the NPs exhibited significant T_1 signal enhancement *in vitro*, *in vivo* T_1 MR imaging of 4T1 tumor-bearing mice was conducted before and after intravenous injection of ^{64}Cu-NOTA-Mn_3O_4@PEG-TRC105 (Targeted group) and ^{64}Cu-NOTA-Mn_3O_4@PEG (Non-Targeted group (N-Targeted)) solution at a dose of 20 mg/kg nanoparticles. A positive T_1 signal enhancement in the tumor was observed at 6 h post-injection of ^{64}Cu-NOTA-Mn_3O_4@PEG-TRC105, compared with the same mice prior to the injection of the nanoparticles (Figure 6a). On the contrary, the non-targeted group exhibited slight T_1 signal enhancement in the tumor. Furthermore, in the blocking group, mice were intravenously injected with TRC105 first and then ^{64}Cu-NOTA-Mn_3O_4@PEG-TRC105 (20 mg/kg body weight). At 6 h post injection, the T_1-weighted MR signal in the blocking group

tumors also exhibited slight enhancement and the signal to noise ratio of the T_1-MR in the tumor was about 3 times lower than that only injected with ^{64}Cu-NOTA-Mn_3O_4@PEG-TRC105 (Figure 6b and b, $p < 0.05$), indicating that excess TRC105 blocked the CD105 binding sites, thereby limiting the binding of ^{64}Cu-NOTA-Mn_3O_4@PEG-TRC105, consistent with the PET result at the same time point. Of note, the metabolism pathway for a large nanoparticle such as that evaluated herein is different from many commercially-available MRI contrast agents such as gadolinium chelates. Thus, the timescales of contrast enhancement are expected to be different, with large nanoparticles taking a longer time to accumulate in the tumor than small molecules.

3.6. Histology

Histological studies were conducted to certify that ^{64}Cu-NOTA-Mn_3O_4@PEG-TRC105 was targeted to the tumor vasculature via CD105, as PET and MRI only reflect the distribution of ^{64}Cu and Mn ions but not the Mn_3O_4 conjugated NPs per se. As indicated in Figure 7, the distribution of ^{64}Cu-NOTA-Mn_3O_4@PEG-TRC105 in the 4T1 tumor was primarily on the vasculature, as indicated by the co-localization of the signals for the nanoparticle and CD31. Due to the relatively large size of ^{64}Cu-NOTA-Mn_3O_4@PEG-TRC105, little extravasation was observed in the tumors. In addition, the nanoparticle-related signal in the liver was mostly outside the vasculature, indicating that ^{64}Cu-NOTA-Mn_3O_4@PEG-TRC105 was intercepted by the liver through non-specific RES uptake rather than CD105 targeting. Meanwhile, little nanoparticle accumulation was observed in muscle tissues, in accordance with the results of PET imaging and biodistribution studies.

3.7. Toxicity of Mn_3O_4 conjugated NPs in healthy mice

To investigate the potential *in vivo* toxicity of Mn_3O_4@PEG NPs, histological assessment was carried out by injecting Mn_3O_4@PEG NPs (20 mg/kg) to healthy BALB/c mice via the tail vein. PBS injections served as the control. As shown in Figure 8a, no clear tissue or cellular damage was observed in all major organs of mice, as compared to that obtained from the control group. Serum biochemistry assays were then also conducted to investigate the influence of Mn_3O_4@PEG NPs, especially on potential hepatic injury and kidney functions (Figure 8b). Analysis of four primary hepatic function indicators including aspartate aminotransferase (AST), alanine aminotransferase (ALT), alkaline phosphatase (ALP), and total bilirubin (TBIL), as well as two kidney function indicators including serum creatinine (CREA) and serum urea (UREA), demonstrated no obvious hepatic or kidney disorders in both the mice treated with Mn_3O_4@PEG NPs and the control injected with PBS on both Day 7 and Day 14 post-injection. These results suggested that Mn_3O_4@PEG NPs demonstrated no obvious toxicity in mice and may be a safe agent for tumor imaging.

4. CONCLUSION

We herein report a biocompatible T_1-MRI and PET contrast agent for *in vivo* tumor vasculature targeting based on Mn_3O_4 conjugated NPs, with Cu-64 as the radiolabel and TRC105 as the targeting ligand. CD105, as the specific receptor of TRC105, has been proven to be overexpressed in many proliferating tumor endothelial cells, making it suitable for tumor diagnosis and potential treatment through the use of nanomaterials. The Mn_3O_4

conjugated NPs (^{64}Cu-NOTA-Mn_3O_4@PEG-TRC105) exhibited good radiostability and high specificity for tumor targeting. Bimodal PET/MRI imaging demonstrated that ^{64}Cu-NOTA-Mn_3O_4@PEG-TRC105 accumulated in tumor sites rapidly, peaking at 6 h p.i. and remaining stable over time. Importantly, *in vivo* toxicity investigations revealed that the Mn_3O_4 NPs could be used as a safe nanoplatform for long-term targeted tumor imaging, diagnosis, and therapy.

Supplementary Material

Refer to Web version on PubMed Central for supplementary material.

Acknowledgments

Funding Sources

This work was supported, in part, by the University of Wisconsin-Madison, the National Institutes of Health (NIBIB/NCI 1R01CA169365, 1R01CA205101, 1R01EB021336, T32GM008505, T32CA009206, and P30CA014520), the American Cancer Society (125246-RSG-13-099-01-CCE), the National Natural Science Foundation of China under Grant Nos. 81227901, 11727813, 81571725, 81230033, 31371006, 61405149, 81660505 and 81627807, the Natural Science Basic Research Plan in Shaanxi Province of China under Grant No. 2017JM8057, and the Fundamental Research Funds for the Central Universities (JB171204).

References

1. McDonald DM, Choyke PL. Imaging of Angiogenesis: from Microscope to Clinic. Nat Med. 2003; 9(6):713–725. DOI: 10.1038/Nm0603-713 [PubMed: 12778170]
2. Na HB, Song IC, Hyeon T. Inorganic Nanoparticles for MRI Contrast Agents. Adv Mater. 2009; 21(21):2133–2148. DOI: 10.1002/adma.200802366
3. Weissleder R, Pittet MJ. Imaging in The Era of Molecular Oncology. Nature. 2008; 452(7187):580–589. DOI: 10.1038/nature06917 [PubMed: 18385732]
4. Gambhir SS. Molecular Imaging of Cancer with Positron Emission Tomography. Nat Rev Cancer. 2002; 2(9):683–693. DOI: 10.1038/nrc882 [PubMed: 12209157]
5. Judenhofer MS, Wehrl HF, Newport DF, Catana C, Siegel SB, Becker M, Thielscher A, Kneilling M, Lichy MP, Eichner M, Klingel K, Reischl G, Widmaier S, Rocken M, Nutt RE, Machulla HJ, Uludag K, Cherry SR, Claussen CD, Pichler BJ. Simultaneous PET-MRI: A New Approach for Functional and Morphological Imaging. Nat Med. 2008; 14(4):459–465. DOI: 10.1038/nm1700 [PubMed: 18376410]
6. Glaus C, Rossin R, Welch MJ, Bao G. In Vivo Evaluation of Cu-64-Labeled Magnetic Nanoparticles as a Dual-Modality PET/MR Imaging Agent. Bioconjugate Chem. 2010; 21(4):715–722. DOI: 10.1021/bc900511j
7. Pichler BJ, Kolb A, Nagele T, Schlemmer HP. PET/MRI: Paving the Way for the Next Generation of Clinical Multimodality Imaging Applications. J Nucl Med. 2010; 51(3):333–336. DOI: 10.2967/jnumed.109.061853 [PubMed: 20150252]
8. Kim J, Piao Y, Hyeon T. Multifunctional Nanostructured Materials for Multimodal Imaging, and Simultaneous Imaging and Therapy. Chem Soc Rev. 2009; 38(2):372–390. DOI: 10.1039/b709883a [PubMed: 19169455]
9. Lee H, Lee E, Kim DK, Jang NK, Jeong YY, Jon S. Antibiofouling Polymer-Coated Superparamagnetic Iron Oxide Nanoparticles as Potential Magnetic Resonance Contrast Agents for in Vivo Cancer Imaging. J Am Chem Soc. 2006; 128(22):7383–7389. DOI: 10.1021/ja061529k [PubMed: 16734494]
10. Ma LL, Feldman MD, Tam JM, Paranjape AS, Cheruku KK, Larson TA, Tam JO, Ingram DR, Paramita V, Villard JW, Jenkins JT, Wang T, Clarke GD, Asmis R, Sokolov K, Chandrasekar B, Milner TE, Johnston KP. Small Multifunctional Nanoclusters (Nanoroses) for Targeted Cellular

Imaging and Therapy. Acs Nano. 2009; 3(9):2686–2696. DOI: 10.1021/nn900440e [PubMed: 19711944]

11. Wong RM, Gilbert DA, Liu K, Louie AY. Rapid Size-Controlled Synthesis of Dextran-Coated, Cu-64-Doped Iron Oxide Nanoparticles. Acs Nano. 2012; 6(4):3461–3467. DOI: 10.1021/nn300494k [PubMed: 22417124]
12. Yang XQ, Hong H, Grailer JJ, Rowland IJ, Javadi A, Hurley SA, Xiao YL, Yang YA, Zhang Y, Nickles R, Cai WB, Steeber DA, Gong SQ. cRGD-Functionalized, DOX-Conjugated, and Cu-64-Labeled Superparamagnetic Iron Oxide Nanoparticles for Targeted Anticancer Drug Delivery and PET/MR Imaging. Biomaterials. 2011; 32(17):4151–4160. DOI: 10.1016/j.biomaterials.2011.02.006 [PubMed: 21367450]
13. Na HB, Hyeon T. Nanostructured T1 MRI Contrast Agents. J Mater Chem. 2009; 19(35):6267–6273. DOI: 10.1039/b902685a
14. Xiao J, Tian XM, Yang C, Liu P, Luo NQ, Liang Y, Li HB, Chen DH, Wang CX, Li L, Yang GW. Ultrahigh Relaxivity and Safe Probes of Manganese Oxide Nanoparticles for *in Vivo* Imaging. Sci Rep. 2013; 3:3424.doi: 10.1038/srep03424 [PubMed: 24305731]
15. Crossgrove J, Zheng W. Manganese Toxicity upon Overexposure. Nmr Biomed. 2004; 17(8):544–553. DOI: 10.1002/nbm.931 [PubMed: 15617053]
16. Yu T, Moon J, Park J, Park YI, Na HB, Kim BH, Song IC, Moon WK, Hyeon T. Various-Shaped Uniform Mn3O4 Nanocrystals Synthesized at Low Temperature in Air Atmosphere. Chem Mater. 2009; 21(11):2272–2279. DOI: 10.1021/cm900431b
17. Na HB, Lee JH, An KJ, Park YI, Park M, Lee IS, Nam DH, Kim ST, Kim SH, Kim SW, Lim KH, Kim KS, Kim SO, Hyeon T. Development of a T-1 Contrast Agent for Magnetic Resonance Imaging Using MnO Nanoparticles. Angew Chem Int Edit. 2007; 46(28):5397–5401. DOI: 10.1002/anie.200604775
18. Jun YW, Lee JH, Cheon J. Chemical Design of Nanoparticle Probes for High-Performance Magnetic Resonance Imaging. Angew Chem Int Edit. 2008; 47(28):5122–5135. DOI: 10.1002/anie.200701674
19. Bennewitz MF, Lobo TL, Nkansah MK, Ulas G, Brudvig GW, Shapiro EM. Biocompatible and pH-Sensitive PLGA Encapsulated MnO Nanocrystals for Molecular and Cellular MRI. Acs Nano. 2011; 5(5):3438–3446. DOI: 10.1021/nn1019779 [PubMed: 21495676]
20. Ha TL, Kim HJ, Shin J, Im GH, Lee JW, Heo H, Yang J, Kang CM, Choe YS, Lee JH, Lee IS. Development of Target-Specific Multimodality Imaging Agent by Using Hollow Manganese Oxide Nanoparticles as A Platform. Chem Commun. 2011; 47(32):9176–9178. DOI: 10.1039/c1cc12961a
21. Hao R, Yu J, Hou YL, Sun SH. One-Pot Synthesis of Hollow/Porous Mn-Based Nanoparticles via a Controlled Ion Transfer Process. Chem Commun. 2011; 47(32):9095–9097. DOI: 10.1039/c1cc12759d
22. Shin JM, Anisur RM, Ko MK, Im GH, Lee JH, Lee IS. Hollow Manganese Oxide Nanoparticles as Multifunctional Agents for Magnetic Resonance Imaging and Drug Delivery. Angew Chem Int Edit. 2009; 48(2):321–324. DOI: 10.1002/anie.200802323
23. Huang CC, Khu NH, Yeh CS. The Characteristics of Sub 10 nm Manganese Oxide T-1 Contrast Agents of Different Nanostructured Morphologies. Biomaterials. 2010; 31(14):4073–4078. DOI: 10.1016/j.biomaterials.2010.01.087 [PubMed: 20149451]
24. Huang J, Xie J, Chen K, Bu LH, Lee S, Cheng Z, Li XG, Chen XY. HSA Coated MnO Nanoparticles with Prominent MRI Contrast for Tumor Imaging. Chem Commun. 2010; 46(36):6684–6686. DOI: 10.1039/c0cc01041c
25. Yang XY, Zhou ZG, Wang L, Tang CZ, Yang H, Yang SP. Folate Conjugated Mn3O4@SiO2 Nanoparticles for Targeted Magnetic Resonance Imaging in Vivo. Mater Res Bull. 2014; 57:97–102. DOI: 10.1016/j.materresbull.2014.05.023
26. Hu H, Dai AT, Sun J, Li XY, Gao FH, Wu LZ, Fang Y, Yang H, An L, Wu HX, Yang SP. Aptamer-Conjugated Mn3O4@SiO2 Core-Shell Nanoprobes for Targeted Magnetic Resonance Imaging. Nanoscale. 2013; 5(21):10447–10454. DOI: 10.1039/c3nr03490a [PubMed: 24057072]
27. Yang H, Zhuang YM, Hu H, Du XX, Zhang CX, Shi XY, Wu HX, Yang SP. Silica-Coated Manganese Oxide Nanoparticles as a Platform for Targeted Magnetic Resonance and Fluorescence

Imaging of Cancer Cells. Adv Funct Mater. 2010; 20(11):1733–1741. DOI: 10.1002/adfm.200902445

28. Ruoslahti E, Bhatia SN, Sailor MJ. Targeting of Drugs and Nanoparticles to Tumors. J Cell Biol. 2010; 188(6):759–768. DOI: 10.1083/jcb.200910104 [PubMed: 20231381]
29. Hong H, Zhang Y, Sun JT, Cai WB. Molecular Imaging and Therapy of Cancer with Radiolabeled Nanoparticles. Nano Today. 2009; 4(5):399–413. DOI: 10.1016/j.nantod.2009.07.001 [PubMed: 20161038]
30. Cai WB, Chen XY. Nanoplatforms for Targeted Molecular Imaging in Living Subjects. Small. 2007; 3(11):1840–1854. DOI: 10.1002/smll.200700351 [PubMed: 17943716]
31. Hanahan D, Weinberg RA. The Hallmarks of Cancer. Cell. 2000; 100(1)(00):57–70. 81683–9. DOI: 10.1016/S0092-8674 [PubMed: 10647931]
32. Fonsatti E, Nicolay HJM, Altomonte M, Covre A, Maio M. Targeting Cancer Vasculature via Endoglin/CD105: A Novel Antibody-Based Diagnostic and Therapeutic Strategy in Solid Tumours. Cardiovasc Res. 2010; 86(1):12–19. DOI: 10.1093/cvr/cvp332 [PubMed: 19812043]
33. Seon BK, Haba A, Matsuno F, Takahashi N, Tsujie M, She XW, Harada N, Uneda S, Tsujie T, Toi H, Tsai H, Haruta Y. Endoglin-Targeted Cancer Therapy. Curr Drug Deliv. 2011; 8(1):135–143. [PubMed: 21034418]
34. Zhang Y, Yang YA, Cai WB. Multimodality Imaging of Integrin alpha(v)beta(3) Expression. Theranostics. 2011; 1:135–148. DOI: 10.7150/thno/v01p0135 [PubMed: 21547156]
35. Quon A, Gambhir SS. FDG-PET and Beyond: Molecular Breast Cancer Imaging. J Clin Oncol. 2005; 23(8):1664–1673. DOI: 10.1200/Jco.2005.11.024 [PubMed: 15755974]
36. Engle JW, Hong H, Zhang Y, Valdovinos HF, Myklejord DV, Barnhart TE, Theuer CP, Nickles RJ, Cai WB. Positron Emission Tomography Imaging of Tumor Angiogenesis with a Ga-66-Labeled Monoclonal Antibody. Mol Pharmaceut. 2012; 9(5):1441–1448. DOI: 10.1021/mp300019c
37. Dallas NA, Samuel S, Xia L, Fan F, Gray MJ, Lim SJ, Ellis LM. Endoglin (CD105): A Marker of Tumor Vasculature and Potential Target for Therapy. Clin Cancer Res. 2008; 14(7):1931–1937. DOI: 10.1158/1078-0432.CCR-07-4478 [PubMed: 18381930]
38. Zhang Y, Yang YN, Hong H, Cai WB. Multimodality Molecular Imaging of CD105 (Endoglin) Expression. Int J Clin Exp Med. 2011; 4(1):32–42. [PubMed: 21394284]
39. Apolo AB, Karzai FH, Trepel JB, Alarcon S, Lee S, Lee MJ, Tomita Y, Cao L, Yu YK, Merino MJ, Madan RA, Parnes HL, Steinberg SM, Rodriguez BW, Seon BK, Gulley JL, Arlen PM, Dawson NA, Figg WD, Dahut WL. A Phase II Clinical Trial of TRC105 (Anti-Endoglin Antibody) in Adults with Advanced/Metastatic Urothelial Carcinoma. Clin Genitourin Canc. 2017; 15(1):77–85. DOI: 10.1016/j.clgc.2016.05.010
40. Rosen LS, Hurwitz HI, Wong MK, Goldman J, Mendelson DS, Figg WD, Spencer S, Adams BJ, Alvarez D, Seon BK, Theuer CP, Leigh BR, Gordon MS. A Phase I First-in-Human Study of TRC105 (Anti-Endoglin Antibody) in Patients with Advanced Cancer. Clin Cancer Res. 2012; 18(17):4820–4829. DOI: 10.1158/1078-0432.CCR-12-0098 [PubMed: 22767667]
41. Zhang Y, Hong H, Severin GW, Engle JW, Yang YA, Goel S, Nathanson AJ, Liu G, Nickles RJ, Leigh BR, Barnhart TE, Cai WB. ImmunoPET and Near-Infrared Fluorescence Imaging of CD105 Expression Using a Monoclonal Antibody Dual-Labeled with Zr-89 and IRDye 800CW. Am J Transl Res. 2012; 4(3):333–346. [PubMed: 22937210]
42. Hong H, Yang K, Zhang Y, Engle JW, Feng LZ, Yang YA, Nayak TR, Goel S, Bean J, Theuer CP, Barnhart TE, Liu Z, Cai WB. In Vivo Targeting Imaging of Tumor Vasculature with Radiolabeled, Antibody-Conjugated Nanographene. Acs Nano. 2012; 6(3):2361–2370. DOI: 10.1021/nn204625e [PubMed: 22339280]
43. Hong H, Zhang Y, Engle JW, Nayak TR, Theuer CP, Nickles RJ, Barnhart TE, Cai WB. In Vivo Targeting Positron Emission Tomography Imaging of Tumor Vasculature with Ga-66-Labeled Nano-Graphene. Biomaterials. 2012; 33(16):4147–4156. DOI: 10.1016/j.biomaterials.2012.02.031 [PubMed: 22386918]
44. Hong H, Zhang Y, Severin GW, Yang YN, Engle JW, Niu G, Nickles RJ, Chen XY, Leigh BR, Barnhart TE, Cai WB. Multimodality Imaging of Breast Cancer Experimental Lung Metastasis with Bioluminescence and a Monoclonal Antibody Dual-Labeled with Zr-89 and IRDye 800CW. Mol Pharmaceut. 2012; 9(8):2339–2349. DOI: 10.1021/mp300277f

45. Guo JT, Hong H, Chen GJ, Shi SX, Zheng QF, Zhang Y, Theuer CP, Barnhart TE, Cai WB, Gong SQ. Image-Guided and Tumor-Targeted Drug Delivery with Radiolabeled Unimolecular Micelles. Biomaterials. 2013; 34(33):8323–8332. DOI: 10.1016/j.biomaterials.2013.07.085 [PubMed: 23932288]
46. Shi SX, Yang K, Hong H, Valdovinos HF, Nayak TR, Zhang Y, Theuer CP, Barnhart TE, Liu Z, Cai WB. Tumor Vasculature Targeting and Imaging in Living Mice with Reduced Graphene Oxide. Biomaterials. 2013; 34(12):3002–3009. DOI: 10.1016/j.biomaterials.2013.01.047 [PubMed: 23374706]
47. Chen F, Hong H, Zhang Y, Valdovinos HF, Shi SX, Kwon GS, Theuer CP, Barnhart TE, Cai WB. In Vivo Tumor Targeting and Image-Guided Drug Delivery with Antibody-Conjugated, Radio labeled Mesoporous Silica Nanoparticles. Acs Nano. 2013; 7(10):9027–9039. DOI: 10.1021/nn403617J [PubMed: 24083623]
48. Zhang YC, Qiao T, Hu XY. Preparation of Mn3O4 Nanocrystallites by Low-Temperature Solvothermal Treatment of Gamma-MnOOH Nanowires. J Solid State Chem. 2004; 177(11): 4093–4097. DOI: 10.1016/j.jssc.2004.05.034
49. Ozkaya T, Baykal A, Kavas H, Koseoglu Y, Toprak MS. A Novel Synthetic Route to Mn(3)O(4) Nanoparticles and Their Magnetic Evaluation. Physica B. 2008; 403(19–20):3760–3764. DOI: 10.1016/j.physb.2008.07.002
50. Chen ZW, Lai JKL, Shek CH. Shape-Controlled Synthesis and Nanostructure Evolution of Single-Crystal Mn3O4 Nanocrystals. Scripta Mater. 2006; 55(8):735–738. DOI: 10.1016/j.scriptamat.2006.05.041
51. Yang LX, Zhu YJ, Tong H, Wang WW, Cheng GF. Low Temperature Synthesis of Mn3O4 Polyhedral Nanocrystals and Magnetic Study. J Solid State Chem. 2006; 179(4):1225–1229. DOI: 10.1016/j.jssc.2006.01.033
52. Chang YQ, Xu XY, Luo XH, Chen CP, Yu DP. Synthesis and Characterization of Mn3O4 Nanoparticles. J Cryst Growth. 2004; 264(1–3):232–236. DOI: 10.1016/j.crysgro.2003.11.117
53. Choi HS, Liu W, Misra P, Tanaka E, Zimmer JP, Ipe BI, Bawendi MG, Frangioni JV. Renal Clearance of Quantum Dots. Nat Biotechnol. 2007; 25(10):1165–1170. DOI: 10.1038/nbt1340 [PubMed: 17891134]

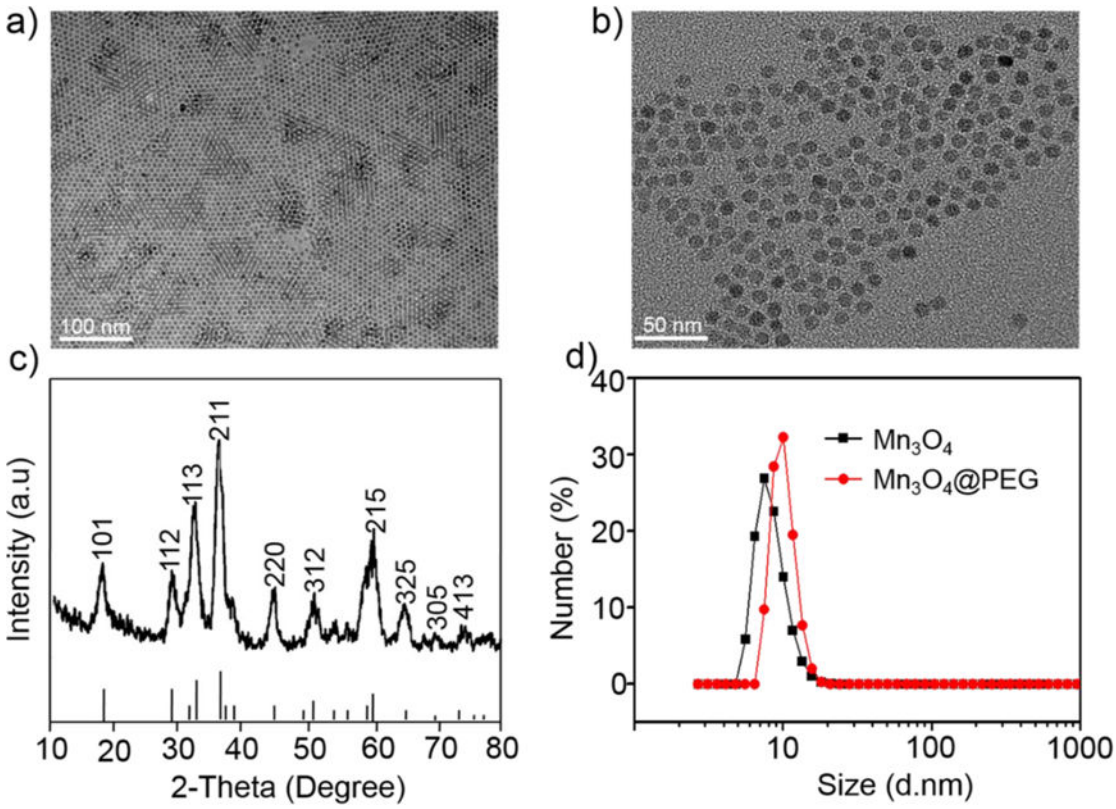

Figure 1.

Characterization of Mn_3O_4@PEG. (a) TEM images of Mn_3O_4 NPs; (b) HRTEM images of Mn_3O_4@PEG NPs; (c) X-ray diffraction pattern of Mn_3O_4 NPs; (d) Size distribution of Mn_3O_4 NPs and Mn_3O_4@PEG as determined through DLS.

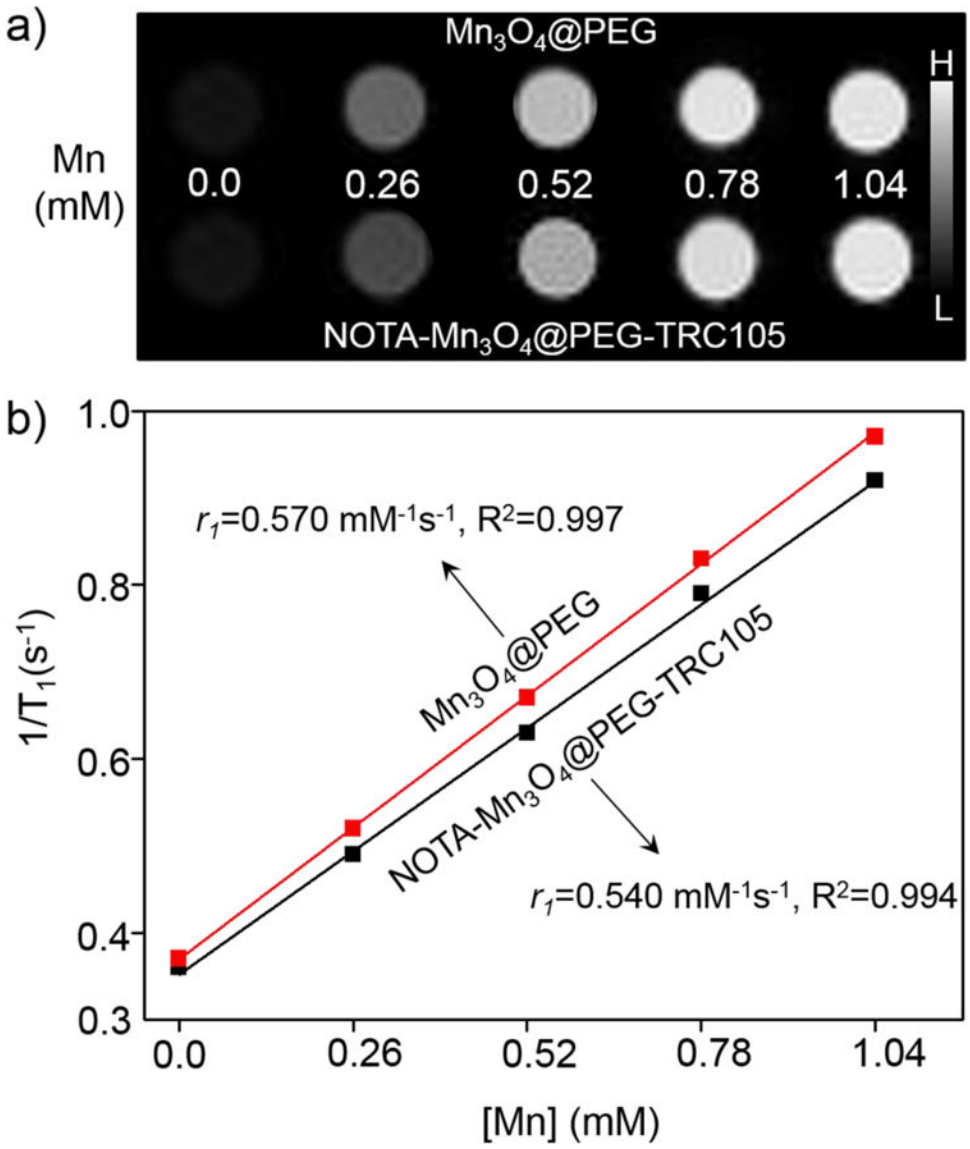

Figure 2.

The relaxation properties of NOTA-Mn_3O_4@PEG-TRC105. (a) T_1-weighted MRI of Mn_3O_4@PEG and NOTA-Mn_3O_4@PEG-TRC105 NPs; (b) T_1 relaxivity plot of aqueous suspensions of Mn_3O_4@PEG and NOTA-Mn_3O_4@PEG-TRC105 NPs on a 4.7 T MRI system.

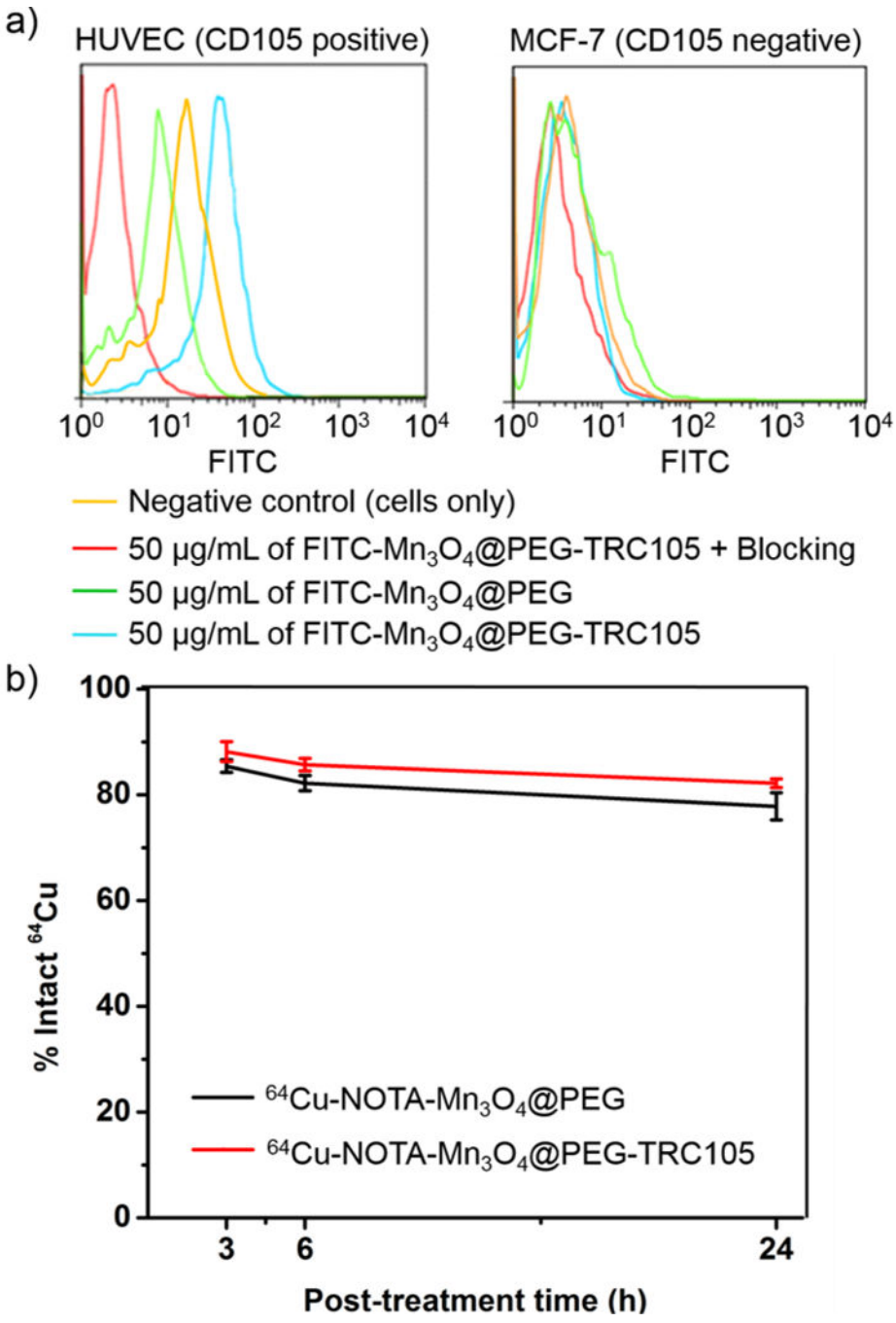

Figure 3.

Flow cytometry analysis and serum stability of Mn_3O_4 conjugated NPs. (a) Flow cytometry analysis of the Mn_3O_4 conjugated NPs in HUVECs (CD105 positive) and MCF-7 breast cancer cells (CD105 negative); (b) Serum stability studies of ^{64}Cu-NOTA-Mn_3O_4@PEG-TRC105 at 37 °C.

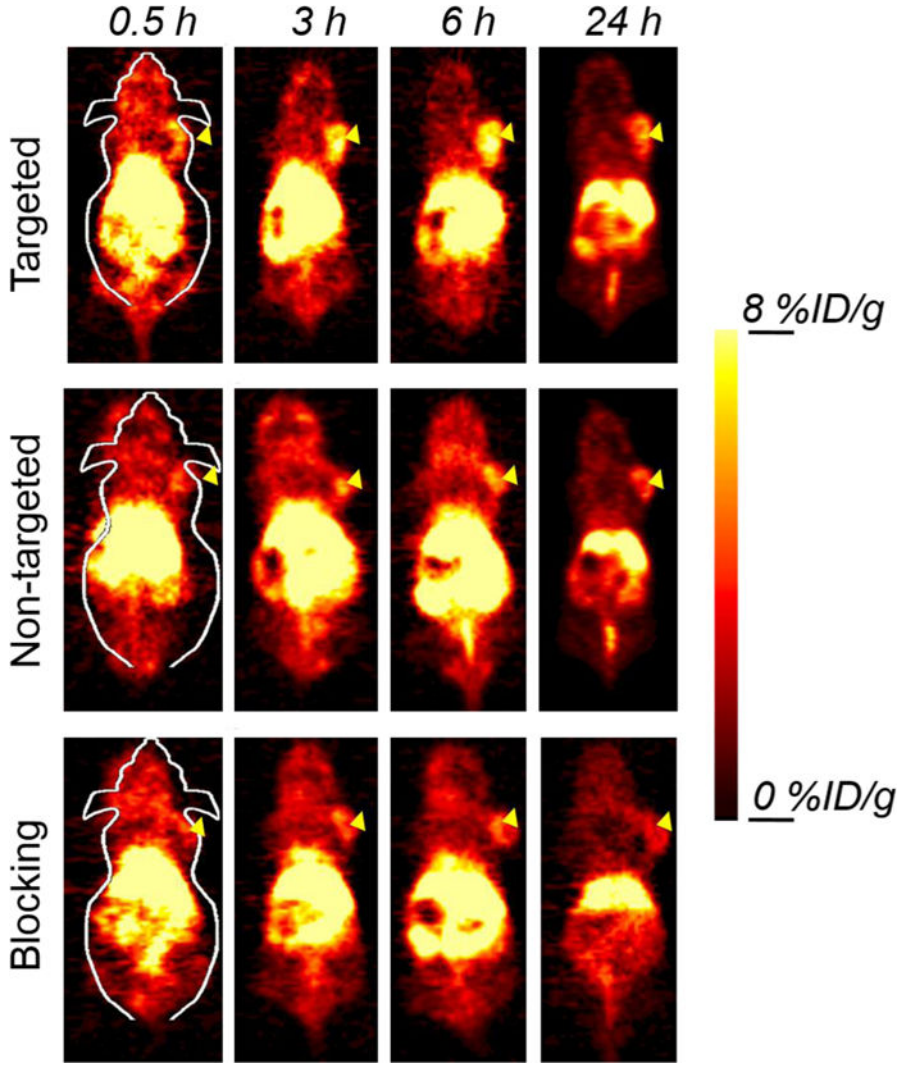

Figure 4.

Serial coronal PET images of 4T1 tumor-bearing mice after injection of ^{64}Cu-NOTA-Mn_3O_4@PEG-TRC105, ^{64}Cu-NOTA-Mn_3O_4@PEG, or ^{64}Cu-NOTA-Mn_3O_4@PEG-TRC105 after a pre-injected blocking dose of TRC105. Arrowheads indicate tumor locations.

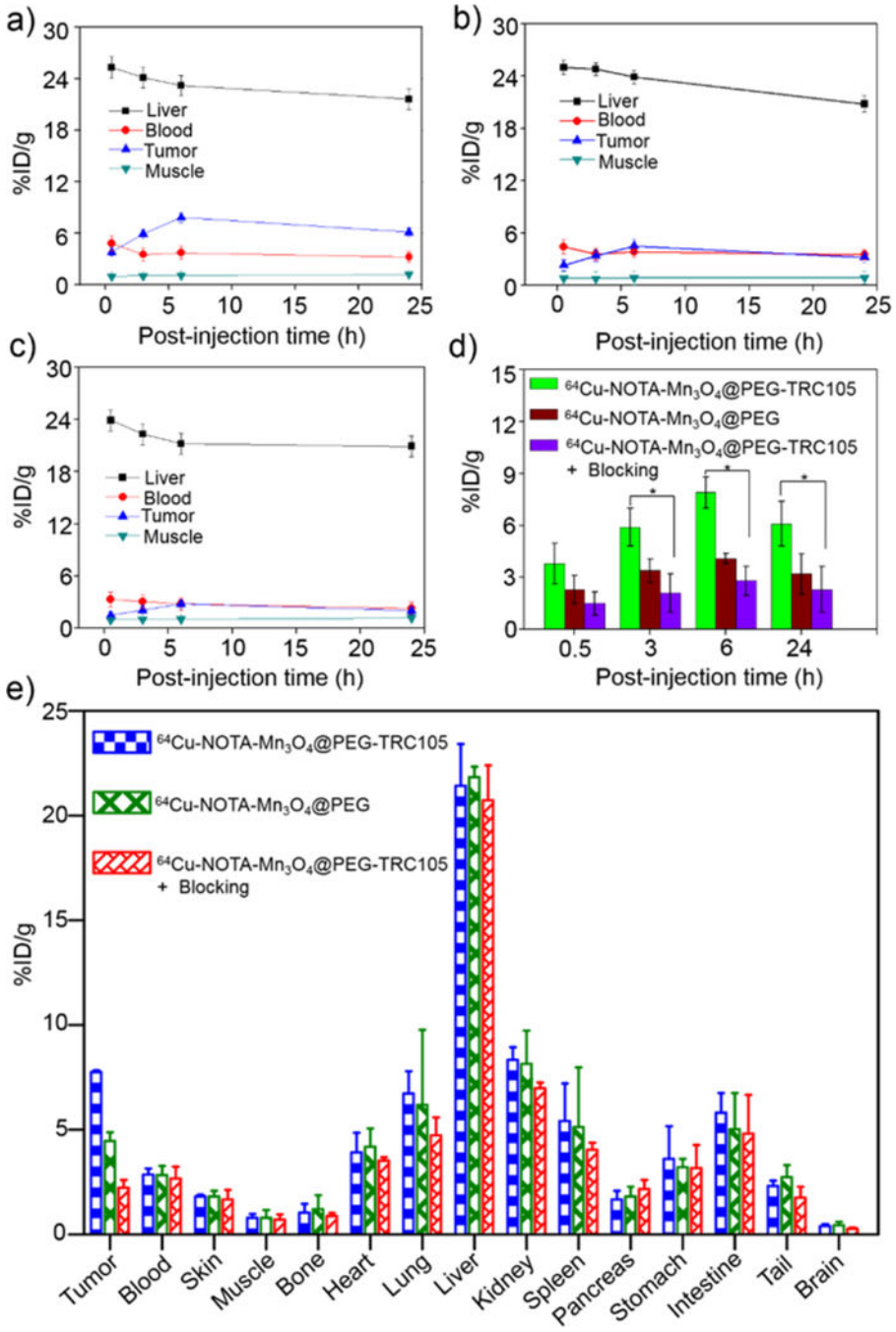

Figure 5.

Quantitative analysis of the PET data. Time-activity curves of the liver, 4T1 tumor, blood, and muscle following intravenous injection of (a) ^{64}Cu-NOTA-Mn_3O_4@PEG-TRC105, (b) non-targeted ^{64}Cu-NOTA-Mn_3O_4@PEG, and (c) ^{64}Cu-NOTA-Mn_3O_4@PEG-TRC105, after a blocking dose of TRC105; (d) 4T1 tumor uptake in the three groups. The differences between uptake in 4T1 tumors of ^{64}Cu-NOTA-Mn_3O_4@PEG-TRC105 and the two control groups were statistically significant ($p < 0.05$) at all time points, except at 0.5 h post-injection between ^{64}Cu-NOTA-Mn_3O_4@PEG-TRC105 and ^{64}Cu-NOTA-Mn_3O_4@PEG (n=3

per group); (e) Biodistribution studies in 4T1 tumor-bearing mice at 24 h post-injection of ^{64}Cu-NOTA-Mn_3O_4@PEG-TRC105, ^{64}Cu-NOTA-Mn_3O_4@PEG and ^{64}Cu-NOTA-Mn_3O_4@PEG-TRC105, after a blocking dose of TRC105 (n=3 per group).

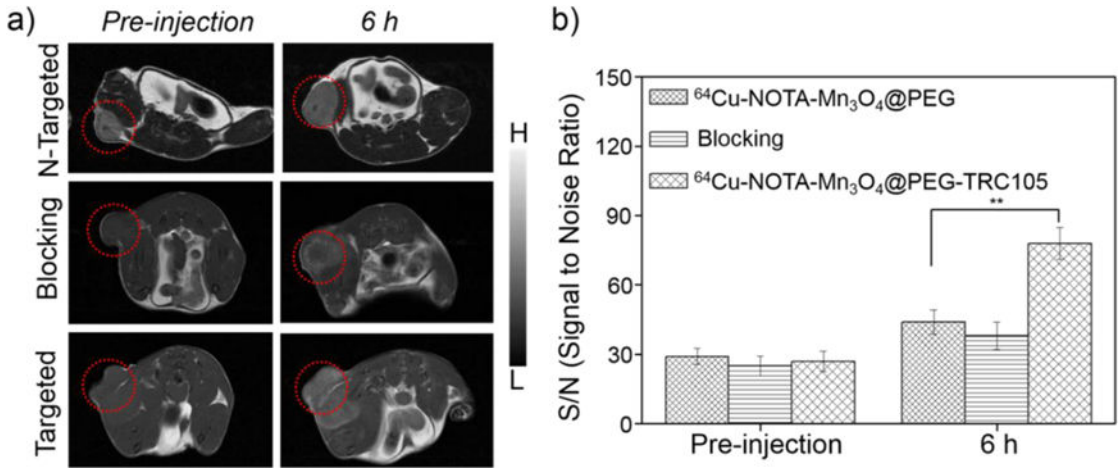

Figure 6.

Serial T_1-weighted MR images of 4T1 tumor-bearing mice. (a) *In vivo* T_1-weighted MRIs acquired prior to and post-injection of ^{64}Cu-NOTA-Mn_3O_4@PEG, ^{64}Cu-NOTA-Mn_3O_4@PEG-TRC105 and ^{64}Cu-NOTA-Mn_3O_4@PEG-TRC105 after a blocking dose of TRC105 (n = 3). Tumors are indicated by circles. (b) The corresponding signal to noise ratio of the tumor before and after intravenous injection of ^{64}Cu-NOTA-Mn_3O_4@PEG, ^{64}Cu-NOTA-Mn_3O_4@PEG-TRC105 and ^{64}Cu-NOTA-Mn_3O_4@PEG-TRC105 after a blocking dose of TRC105.

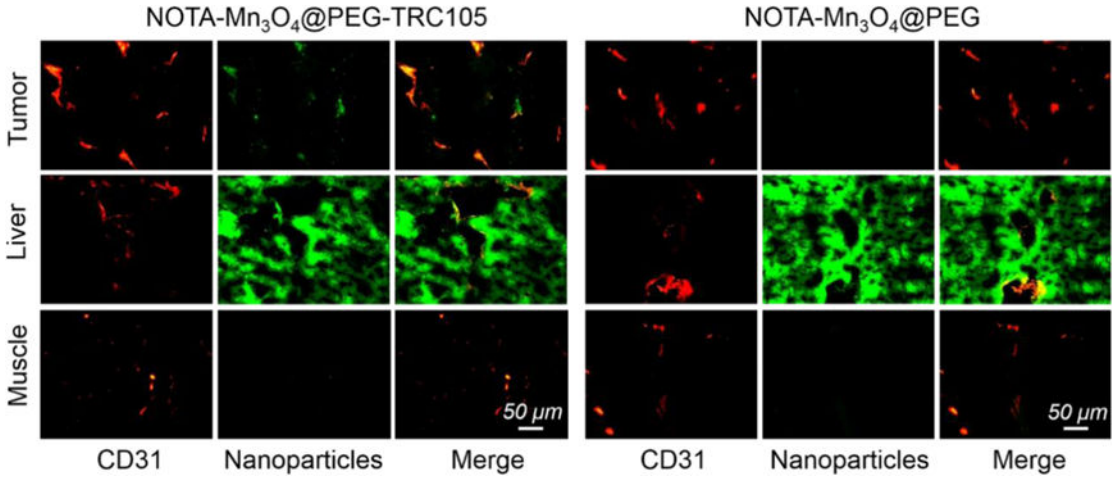

Figure 7.

Immunofluorescent staining for CD31 (red, with anti-mouse CD31 primary antibody) and CD105 (green, using TRC105 within NOTA-Mn_3O_4@PEG-TRC105 as the primary antibody). Magnification: 200×. Scale bar: 50 μm.

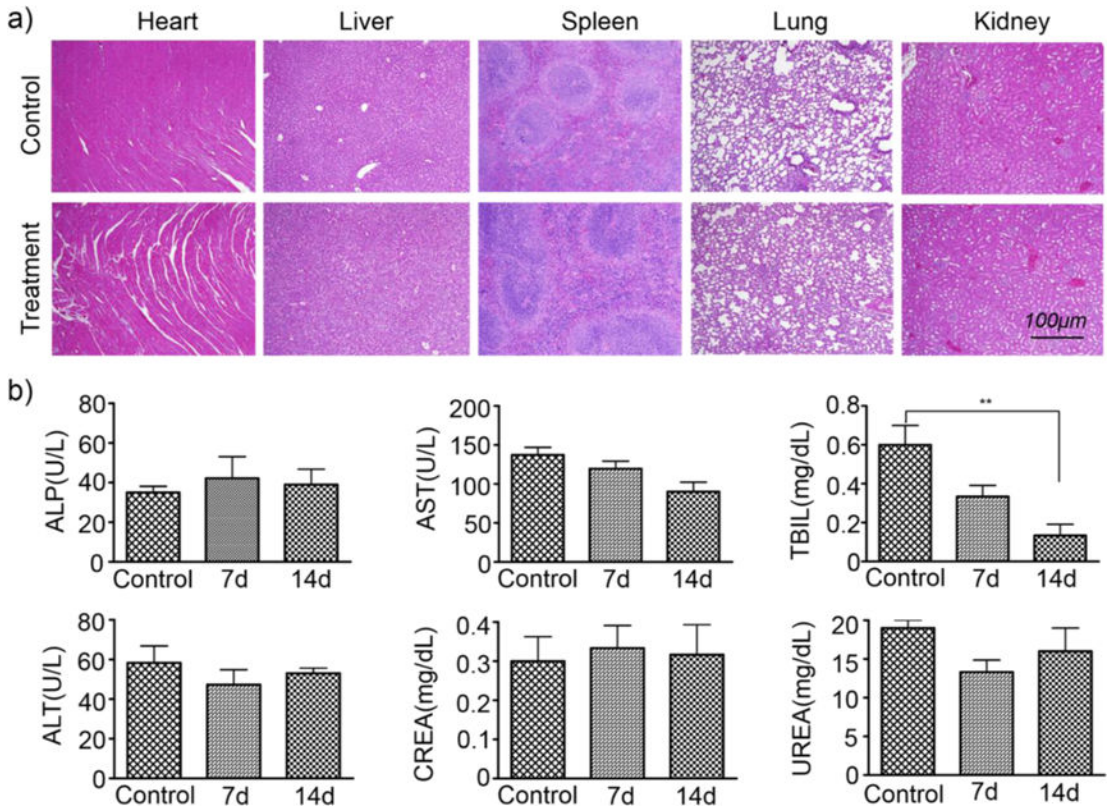

Figure 8.

Biocompatibility studies of Mn_3O_4@PEG in healthy mice.(a) H&E staining of major organs (including heart, liver, spleen, lung, and kidney) from mice after injecting Mn_3O_4@PEG (dose: 20 mg/kg) at 7 d and14 d post-injection. Healthy mice treated with PBS were used as the control. (b) Analysis of liver and kidney function markers. Healthy BALB/c mice were intravenously injected with Mn_3O_4@PEG (dose: 20 mg/kg), and sacrificed on Day 7 and Day 14 post-injection (n = 3).

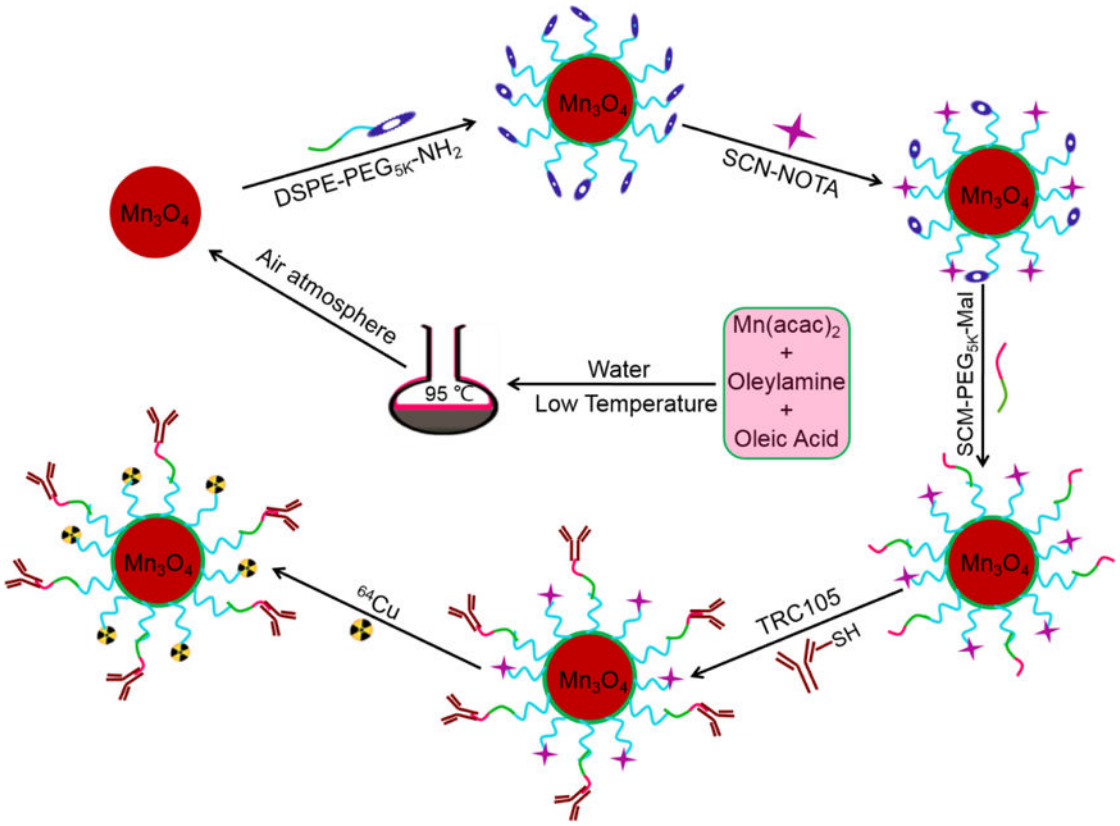

Scheme 1.

Synthesis of the Mn_3O_4 conjugated NPs (^{64}Cu-NOTA-Mn_3O_4@PEG-TRC105).